(Received 14 February 2025, Accepted 25 April 2025, Scheduled 3 May 2025)

Finite Element Boundary Integral Approach for Inhomogeneous-Background Magnetic Resonance Electrical Properties Tomography

(*Invited Paper*)

Yuyue Zhang, Hariharan M. Krishnan, Tiantian Yin, and Xudong Chen*

Department of Electrical and Computer Engineering, National University of Singapore, Singapore 117583, Singapore

ABSTRACT: This paper introduces a novel finite element boundary integral approach for magnetic resonance electrical properties tomography (MR-EPT) with an inhomogeneous background which improves imaging quality by utilizing inhomogeneous background inversion and allows for a flexible selection of areas for fine reconstruction, thereby saving resources and quickly obtaining the most important information. In the proposed approach, a fictitious inhomogeneous background is initialized, followed by a preliminary reconstruction conducted across the entire field of view (FOV) through a few iterations. This fictitious inhomogeneous background aims to enhance the quality of reconstruction, surpassing that achieved through inversion in a homogeneous background. The proposed method is significantly suitable to the prevailing refinement mechanism, where the refinement area identified from the preliminary reconstruction image is embedded in an inhomogeneous background. This method combines the advantages of the computational efficiency of local methods and the noise robustness of global methods. Numerical examples have validated that the inversion with a fictitious inhomogeneous background yields a superior reconstruction quality. The subsequent narrowing of the inversion area results in a more focused inversion process, significantly reducing reconstruction time.

1. INTRODUCTION

Magnetic Resonance Electrical Properties Tomography (MR-EPT) stands as an innovative tomography technique with the capability to quantitatively reconstruct the permittivity and conductivity of biological tissues from Magnetic Resonance Imaging (MRI) signals [1–6].

The retrieval of Electrical Properties (EPs) from the MRI signal is possible due to the information embedded in the signal regarding the interaction between radio frequency (RF) pulses and biological tissues. EPs play a crucial role in estimating biological tissue lesions and determining the local Specific Absorption Rate (SAR).

The knowledge of EPs has the potential to ease the interpretive burden borne by radiologists, aid in formulating hyperthermia therapy treatment plans, and evaluate the safety of the MRI machine.

With the increasing interest of researchers, many methods have been proposed in recent years. These methods can be roughly categorized into differential and integral methods. Differential methods rely on the differential forms of Maxwell's equations [7–14], while integral methods are grounded on their integral counterparts [15–24]. Furthermore, these methods can be classified as either local or global based on the imaging domain they address. The local methods only consider the information of the direct neighborhood to reconstruct the EPs at a specific location [7–10]. In comparison, global methods consider the entire imaging domain to reconstruct the entire EPs map [11–23].

After the initial proposition by Haacke et al. [7] that EPs can be extracted through B_1^+ maps, several methods were introduced, initially leaning towards local differential approaches for their simplicity, such as Helmholtz-based EPT (H-EPT) [8] and simplified H-EPT (SH-EPT) [9]. These methods are under the assumption of local homogeneity in EPs. Subsequently, global differential methods emerged with fewer assumptions, such as gradient-based EPT (G-EPT) [11, 12] and convection-reaction EPT (cr-EPT) [13, 14]. It is acknowledged that differential methods are constrained by their inherent property of noise amplification [2, 3]. To address this limitation, researchers introduced integral methods, widely used in solving inverse scattering problems, into MR-EPT. For example, Balidemaj et al. [15] incorporated the contrast source inversion (CSI) [25, 26] into MR-EPT. Then, Arduino et al. [18] and Leijsen et al. [16] expanded the application of CSI-EPT to phaseless and 3-dimensional cases, respectively. Additionally, Leijsen et al. [19] discussed the performances of CSI-EPT under various circumstances, such as different regularization techniques, initial guesses and noise levels. Meanwhile, Hong et al. [22] introduced the variational Born iteration method [27] into MR-EPT. In addition, as machine learning techniques have advanced, physics-informed neural networks (PINNs) have been incorporated into MR-EPT frame-

* Corresponding author: Xudong Chen (elechenx@nus.edu.sg).

works [28–31]. For example, Inda et al. [28] implemented a neural network to optimize two key coefficients of cr-EPT, in order to reduce artifacts. More broadly, neural network-based approaches have also shown promise in solving inverse scattering problems, including those with phaseless or limited data [32, 33]. Among these methods, CSI-EPT presents notable advantages due to its ability to circumvent locally homogeneous assumptions and eliminate the need for repeated forward simulations. However, it is likely to be trapped in local minima, particularly when the nonlinearity of the problems becomes strong [19, 25, 26]. An appropriate initial guess can significantly reduce the likelihood of being trapped in local minima. Furthermore, achieving a a finer reconstruction requires a finer discretization and more iterations, significantly increasing the reconstruction time.

To provide an effective initial guess and reduce the reconstruction time, this paper proposes a novel approach utilizing a fictitious inhomogeneous background. The motivation behind this approach stems from two perspectives. Firstly, the incorporation of a fictitious inhomogeneous background is employed to enhance the overall quality of reconstruction. The concept of the fictitious inhomogeneous background implies that the background being utilized is not authentic, but instead as a mathematical concept, it is artificially designed to facilitate the reconstruction process. Secondly, the inhomogeneous background inversion allows us to flexibly choose the refinement area, which treats the exterior of the refinement area as a fixed inhomogeneous background, serves to narrow the inversion domain from the entire field of view (FOV) to the refinement area, thereby improving the efficiency of the inversion process. While the concept of using a fictitious inhomogeneous background has been studied in other inverse problems, its integration into the MR-EPT framework using a numerically computed Green's function and IE-based CSI formulation is, to the best of our knowledge, novel.

The proposed finite element boundary integral (FE-BI) approach can deal with any inhomogeneous background. The process of this approach can be divided into two stages: the preliminary stage and the refinement stage. The preliminary stage aims to obtain a preliminary result for the refinement stage. The inversion in the preliminary stage is conducted across the entire FOV. The refinement stage, on the other hand, focuses on improving the reconstruction within the refinement area. In the preliminary stage, we first estimate the spatial distribution of EP based on our prior information and treat it as the fictitious inhomogeneous background. Then the values of EP will be gradually tuned so that eventually the calculated data match the measured data. Given the fact that the corresponding Green's function with an inhomogeneous background does not have an analytic expression, the Green's function is numerically computed by the FE-BI formulation. This computation of the numerical Green's function is performed only once and then stored for use in subsequent iterations. Subsequently, an objective function is formulated and iteratively minimized to obtain a preliminary reconstruction. Once a preliminary reconstruction is obtained, the process advances to the refinement stage. A refinement area that requires further refinement is identified by analyzing the preliminary reconstruction image together with other conventional MRI images. Then, the objects outside the refinement area are designated as the fictitious inhomogeneous background in this stage, which is fixed when the interior is further refined. Utilizing Huygens' principle, which states that the field outside the refinement area can be effectively represented by a boundary integral (BI) [34–36], the inversion domain can be narrowed from the entire FOV to the refinement area. Subsequent steps involve recalculating the new inhomogeneous background Green's function and formulating a new objective equation within this refinement area. The reduction in the inversion area leads to a significant reduction in reconstruction time, thereby facilitating a more efficient and adaptable reconstruction process.

The contributions of this paper can be briefly summarized as follows:

1) Establishing a forward MR-EPT model based on the FE-BI method, this paper provides a model that is more convenient for accommodating inhomogeneous backgrounds and scenarios with a narrowed refinement area. The proposed forward MR-EPT model has the advantage of fully incorporating *a priori* knowledge of imaging domain that is often medically available. The *a priori* knowledge of image domain, which is heterogeneous, provides us with a start point, which is treated as an inhomogeneous background. In addition, our proposed model allows a great flexibility in choosing an inhomogeneous background. It should be highlighted that the difference from previous FEM-CSI [37–40] works lies in our use of a numerically computed inhomogeneous background Green's function, integrated into the CSI cost function instead of directly solving the differential equation, and apply the prior information to the domain of MR-EPT, where such methodology has not yet been explored in the same depth.

   The proposed forward MR-EPT model achieves computational efficiency through a strategic reduction of the computational domain, focusing updates only within regions where property changes are necessary. By applying Huygens' principle, the reconstruction region is effectively isolated from its surroundings, allowing the external environment to be treated as fixed. This approach eliminates the need to repeatedly compute the influence of distant, unchanging areas, thereby significantly reducing computational load. As a result, resources are concentrated on the critical regions of interest, enhancing efficiency without compromising accuracy, in contrast to traditional full-domain methods that require continuous evaluation of the entire area.

2) When building up the objective function of the optimization problem, the paper rewrites the data equation and state equation of the MR-EPT problem to leverage the advantageous properties of the FE-BI formulation handling the inhomogeneous background.

3) The proposed method is significantly suitable for the refinement mechanism, where the refinement area identified from the preliminary reconstruction image is embedded in an inhomogeneous background. By employing Huygens'

principle, the proposed approach can narrow the reconstruction domain, leading to a reduction in reconstruction time. This reduction in the image domain and reconstruction time enhances the flexibility of MR-EPT applications. It should be noted that the proposed refinement mechanism with inhomogeneous background is significantly different from prevailing refinement mechanism.

4) This method combines the advantages of local methods and global methods. Specifically, it only requires the computation of the local meshes during the inversion process to enhance computational efficiency, while also utilizing integral equations to account for the influence of the global meshes on the measured data to improve the robustness against noise.

The structure of this paper is organized as follows. In Section 2 the forward model based on FE-BI is introduced. Section 3 introduces the detailed procedure of the inversion process. In Section 4, numerical examples are conducted and compared. The conclusion is drawn in Section 5.

2. FORWARD MODEL

This section introduces the forward model for both the preliminary stage and the refinement stage. It is important to note that the forward model is similar for both stages, with differences in the computation area and boundaries. Let's consider a two-dimensional (2-D) transverse magnetic (TM) MRI configuration in this paper, as shown in Fig. 1. The RF coils are located in a circular pattern to transmit the RF pulse. Objects within the FOV are activated by the RF pulses, subsequently generating the MR signals captured by the RF coils. The FOV is delineated by the red dashed lines, while the refinement area is marked by the white dashed lines. The positive rotating magnetic field B_1^+ can be mapped through MRI signals by B_1 mapping techniques [41, 42], which is defined as

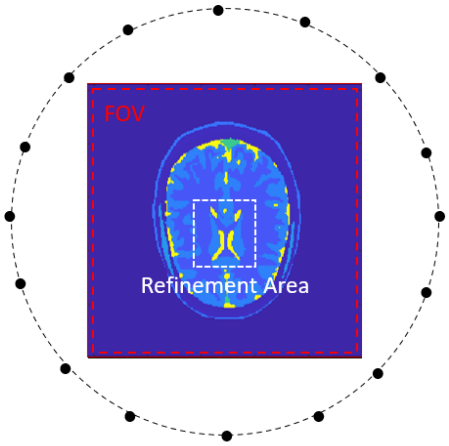

FIGURE 1. In the preliminary stage, the calculation domain encompasses the entire Field Of View (FOV), indicated by the red dashed line. In the refinement stage, the computational domain is restricted to the refinement area, which is marked by the white dashed line.

$$B_1^+(\vec{r}) = \frac{B_x(\vec{r}) + iB_y(\vec{r})}{2}, \quad \vec{r} \in D \tag{1}$$

where B_x and B_y are the x and y components of the magnetic field, respectively, and D denotes the FOV in the preliminary stage and as the refinement area in the refinement stage, respectively. Notably, the measured data, B_1^+, is related to the EPs of objects and is governed by Maxwell's equations. More specifically, given the negligible variations in relative permeability of objects investigated in this paper, B_1^+ is directly related to the permittivity ε and conductivity σ. Therefore, B_1^+ is considered as the measured data in the MR-EPT problem.

In the 2-D TM cases, the electric field only contains z component E_z while the magnetic field contains x and y components B_x and B_y. The objects within FOV are biological tissues with a permittivity $\varepsilon_0\varepsilon_r(\vec{r})$, conductivity $\sigma(\vec{r})$, and permeability $\mu(\vec{r}) = \mu_0$. These tissues are immersed in a background with the permittivity $\varepsilon_0\varepsilon_b(\vec{r})$, conductivity $\sigma_b(\vec{r})$, and permeability μ_0. The EPs of objects and background can be expressed using complex relative permittivities $\tilde{\varepsilon}_r(\vec{r}) = \varepsilon_r(\vec{r}) + i\sigma(\vec{r})/(\omega\varepsilon_0)$ and $\tilde{\varepsilon}_b(\vec{r}) = \varepsilon_b(\vec{r}) + i\sigma_b(\vec{r})/(\omega\varepsilon_0)$ with the time convention $e^{-i\omega t}$ omitted in the following. It is noteworthy that, in reality, the background is air with a relative permittivity of ε_0. However, for the sake of reconstruction facilitation, a fictitious inhomogeneous background with a complex relative permittivity $\tilde{\varepsilon}_b(\vec{r})$ can be reasonably estimated using prior information, such as the MRI image obtained through conventional methods. It is worth highlighting that the value of $\tilde{\varepsilon}_b(\vec{r})$ is not required to be accurate, since the formula $\tilde{\varepsilon}_r(\vec{r}) = \tilde{\varepsilon}_b(\vec{r}) + [\tilde{\varepsilon}_r(\vec{r}) - \tilde{\varepsilon}_b(\vec{r})]$ is always correct, i.e., we treat $\tilde{\varepsilon}_r(\vec{r}) - \tilde{\varepsilon}_b(\vec{r})$ as the perturbation in the background medium $\tilde{\varepsilon}_b(\vec{r})$.

In the interior domain of D, the electrical field is governed by the Helmholtz equation, which can be written as

$$\nabla^2 E_z(\vec{r}) + k_0^2 \tilde{\varepsilon}_r(\vec{r}) E_z(\vec{r}) = 0 \tag{2}$$

$$\nabla^2 E_z^i(\vec{r}) + k_0^2 \tilde{\varepsilon}_b(\vec{r}) E_z^i(\vec{r}) = 0 \tag{3}$$

where k_0 represents the wave number of the free space, and E_z and E_z^i denote the electrical field with and without the presence of objects, respectively.

Subtracting Equation (2) with Equation (3) yields

$$\nabla^2 E_z^s(\vec{r}) + k_0^2 \tilde{\varepsilon}_b(\vec{r}) E_z^s(\vec{r}) = -k_0^2 [\tilde{\varepsilon}_r(\vec{r}) - \tilde{\varepsilon}_b(\vec{r})] E_z(\vec{r}) \tag{4}$$

where $E_z^s = E_z - E_z^i$ denotes the scattered electrical field.

Let's define the right hand of Equation (4) to be the contrast source $w(\vec{r})$, there is

$$w(\vec{r}) = \chi(\vec{r}) E_z(\vec{r}) = -k_0^2 [\tilde{\varepsilon}_r(\vec{r}) - \tilde{\varepsilon}_b(\vec{r})] E_z(\vec{r}) \tag{5}$$

where $\chi(\vec{r}) = -k_0^2[\tilde{\varepsilon}_r(\vec{r}) - \tilde{\varepsilon}_b(\vec{r})]$ represents the contrast. It is obvious that the value of contrast is related to the predefined background, which can be either a fictitious inhomogeneous background or a homogeneous background. Once the contrast is obtained, the permittivity of objects can be determined by $\tilde{\varepsilon}_r(\vec{r}) = \tilde{\varepsilon}_b(\vec{r}) + [\tilde{\varepsilon}_r(\vec{r}) - \tilde{\varepsilon}_b(\vec{r})]$. The above equation applies to both stages.

In the exterior of the boundary, employing Huygens' principle, the field can be written as [34, 43]

$$E_z^s(l) = \oint_{\partial D} -\frac{\partial E_z^s(l')}{\partial n(l')} G(l,l') + \frac{\partial G(l')}{\partial n(l')} E_z^s(l') dl' \quad l,l' \in \partial D \tag{6}$$

where G represents the Green's function mapping the source on the boundary to the corresponding fields on the boundary, and $\hat{n}$ denotes the normal vector pointing outward from the boundary of ∂D. In the preliminary stage, the boundary of ∂D is the red dashed line in the Fig. 1. Outside the boundary is air, so G is the free space Green's function, since (6) is considered as approaching the boundary from the external region. That is to say, the Green's function G in (6) accounts for the external electromagnetic response. In the refinement stage, the boundary marked by the white dashed line is located inside the object, so G is the inhomogeneous background Green's function that needs to be calculated numerically.

As mentioned above, the measured data in the MR-EPT problem is B_1^+, and the scattered part of B_1^+ is defined as

$$B_1^{+,s}(\vec{r}) = B_1^+(\vec{r}) - B_1^{+,i}(\vec{r}) \tag{7}$$

where B_1^+ and $B_1^{+,i}$ represent the positive rotating magnetic field with and without the presence of objects, respectively.

After discretizing the domain D into a total of N_{mesh} meshes with a total of N_{node} nodes and expanding the variables with the bilinear basis function, we obtain the discrete form of $B_1^{+,s}$, derived from (3)–(7) in FE method,

$$\bar{B}_1^{+,s} = \bar{\bar{P}} \cdot \bar{\bar{G}}_D \cdot \bar{w} \tag{8}$$

where $\bar{\bar{P}}$ is an $N_{mesh} \times N_{node}$ matrix that maps the scattered electrical field at the nodes of meshes to the $\bar{B}_1^{+,s}$ located at the center of the meshes; $\bar{\bar{G}}_D$ is an $N_{node} \times N_{node}$ matrix that represents the inhomogeneous Green's function that maps the contrast source at the nodes to the electrical field at the nodes; and $\bar{w}$ is an N_{node} dimensional vector that denotes the value of the contrast source of each node.

The crucial step of the forward process involves determining the inhomogeneous Green's function $\bar{\bar{G}}_D$. The approach involves treating the inhomogeneous background as scatterers within a homogeneous background and computing $\bar{\bar{G}}_D$ using the forward solver. The detailed derivation and the expressions of matrices $\bar{\bar{P}}$ and $\bar{\bar{G}}_D$ can be referred to Appendix A. It should be highlighted that for a given inhomogeneous background, the $\bar{\bar{G}}_D$ needs to be computed only once, which does not significantly increase the computational burden.

3. INVERSION PROCESS

As highlighted in the introduction, the motivation for this approach originates from two perspectives. Firstly, the formulation of inhomogeneous background inversion is introduced. Secondly, the workflow of the refinement-based inversion is presented.

3.1. Inhomogeneous Background Inversion

In this paper, the inversion problem is recast as an optimization problem [15–17, 25] and is addressed through iterative minimization of an objective function. The objective function in this approach is organized by two equations: the data equation and the state equation.

The data equation illustrates the relation between the measured data and the contrast source, as illustrated in (8). In comparison, the state equation illustrates the physics governing the interaction between the incident waves and the objects, which can be formulated as

$$\bar{\bar{C}} \cdot \bar{w} = \bar{\bar{\chi}} \cdot \bar{\bar{C}} \cdot (\bar{E}_z^i + \bar{\bar{G}}_D \cdot \bar{w}) \tag{9}$$

where $\bar{\bar{C}}$ is a matrix with dimensions $N_{mesh} \times N_{node}$ that assigns the value of the center of a mesh by averaging the values at their four respective nodes; $\bar{\bar{\chi}}$ is a diagonal matrix of dimension $N_{mesh} \times N_{mesh}$, where its diagonal elements represent the contrast associated with each mesh; and $\bar{E}_z^i$ is an N_{node} dimensional vector that denotes the value of incident electrical field at each node. The meaning of (9) can be interpreted as enforcing (5) at the center of each mesh.

Thus, the relative residual for the data Equation (8) and the state Equation (9) are defined as

$$\Delta_{dat} = \frac{\| \bar{B}_1^{+,s} - \bar{\bar{P}} \cdot \bar{\bar{G}}_D \cdot \bar{w} \|^2}{\| \bar{B}^{+,s} \|^2} \tag{10}$$

$$\Delta_{sta} = \frac{\| \bar{\bar{C}} \cdot \bar{w} - \bar{\bar{\chi}} \cdot \bar{\bar{C}} \cdot (\bar{E}_z^i + \bar{\bar{G}}_D \cdot \bar{w}) \|^2}{\| \bar{\bar{\chi}} \cdot \bar{E}_z^i \|^2} \tag{11}$$

respectively. Then, the objective function is organized as

$$\mathcal{F}(w, \chi) = \Delta_{dat} + \Delta_{sta} \tag{12}$$

It is evident that the unknowns within the objective function are w and χ, both of which can be iteratively updated by minimizing the objective function. Additionally, the inhomogeneous background Green's function $\bar{\bar{G}}_D$ remains fixed and can be computed and stored at the beginning. The conjugate gradient method (CGM) is utilized to minimize the objective function in this paper. It is noteworthy that in MR-EPT, the measured data is available throughout the entire object domain. As a result, the positions of objects can be determined based on the measured data before we run iterations when solving the minimization problem.

3.2. Refinement-Based Inversion

To achieve better reconstructions, it is necessary to employ a fine discretization and run sufficient iterations, which, unfortunately, leads to time-consuming computations. However, in practical situations, not every part of the domain requires equal attention. Focusing specifically on the refinement area, where sufficient iterations are crucial, can significantly reduce the nonlinearity of the inverse problem and the computational time. Therefore, a novel approach is developed to flexibly determine the inversion domain, resulting in a substantial reduction in computational time.

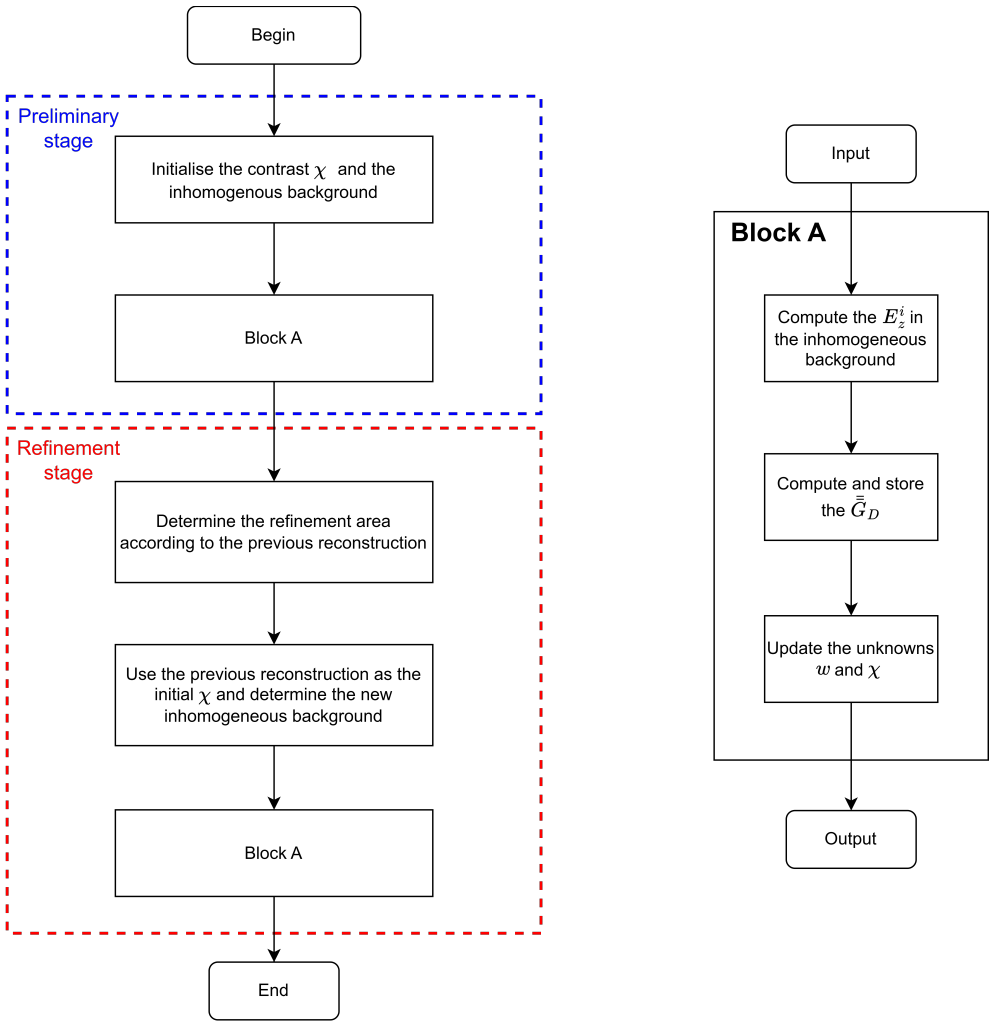

FIGURE 2. Flowchart of the refinement-based inversion.

The workflow of the refinement-based inversion is illustrated in Fig. 2. It can be seen that the process can be divided into two stages. In the preliminary stage, the reconstruction is carried out in the entire FOV. The initial contrast χ and the electrical parameters of the inhomogeneous background are firstly initialized. These initial parameters can be derived from anatomical information and conventional MRI images. For instance, in head imaging, the locations of the skin and skull of the head can be easily identified from conventional MRI images, and approximated EPs values can be assigned accordingly. The remaining portion is chosen as a homogeneous guess with the average expected values of EPs. This initial information serves as the initial fictitious inhomogeneous background. Subsequently, the incident field E_z^i in this inhomogeneous background is computed. Then the inhomogeneous Green's function $\bar{\bar{G}}_D$ mapping the contrast source to the electric field in Equation (8) can be calculated. The unknowns w and χ are then updated through inhomogeneous background inversion, as previously introduced. Given that the inversion domain spans the entire FOV, the dimensions of the matrices of unknowns are considerably large. Consequently, it will be time-consuming if we aim to obtain precise results with an adequate number of iterations. Therefore, to mitigate computational costs, a reduced number of iterations are performed in this inversion process, yielding rough reconstruction results.

Once a preliminary result is obtained, the reconstruction moves to the refinement stage, where the inversion domain is narrowed to the refinement area. The refinement area can be determined based on preliminary results. The preliminary reconstruction result outside the refinement area is fixed and serves as a new inhomogeneous background. The boundary in Equation (6) is correspondingly narrowed from the boundary of the FOV to the boundary of the refinement area, which is enclosed by the white dashed lines in Fig. 1. The influence stemming from scatterers outside this boundary can be represented by electrical and magnetic sources located on the boundary, in accordance with Huygens' principle, which enables a reduction in the inversion domain. It should be noted that Green's function on the boundary in Equation (6) becomes the inhomogeneous background Green's function; therefore, we must calculate the new background Green's function in the refinement stage. Further step involves recalculating E_z^i under the new background. Finally, by minimizing the objective function (12) for the new background medium and new computational domain, the un-

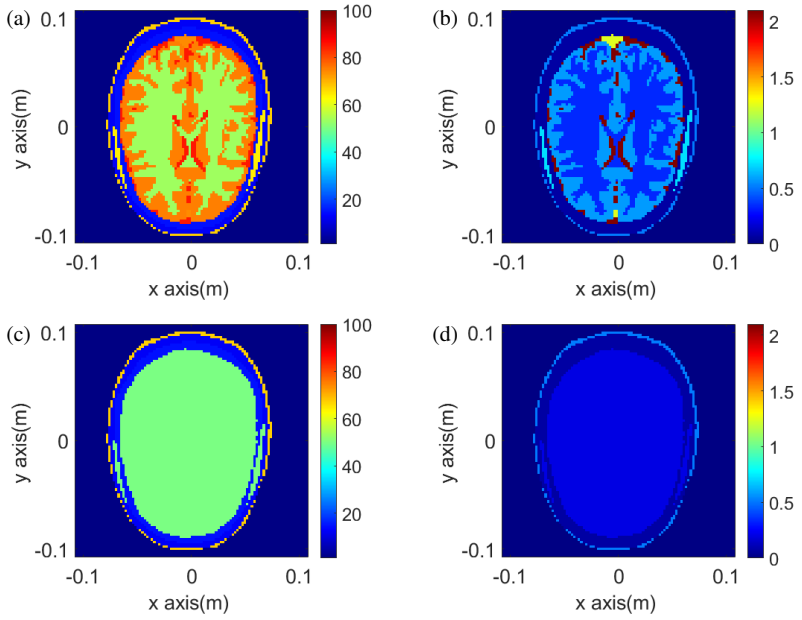

FIGURE 3. The actual values and prior information of permittivity and conductivity of a brain slice. (a) Actual permittivity; (b) Actual conductivity; (c) Prior information of permittivity; (d) Prior information of conductivity.

knowns w and χ within the refinement area are then iteratively updated.

Since the inversion domain is significantly reduced, the reconstruction time is also greatly decreased. It is worth highlighting that the refinement area can be arbitrarily determined within the FOV, enhancing the flexibility of MR-EPT applications. This method can reduce the global inversion domain to a local inversion domain, thus having the advantage of the high computational efficiency of local methods. At the same time, it is based on integral equations, which consider the influence of all scattering objects, ensuring robustness to noise, similar to global methods.

4. NUMERICAL RESULTS

In this section, numerical simulations are conducted to demonstrate the performance of the proposed approach. Illustrated in Fig. 1, 16 RF line sources are placed in a circle with a radius of 0.35 m. These RF sources are driven at 127.74 MHz, aligning with the operating frequency of a 3T MRI system. The object to be reconstructed is a cross-sectional slice of a brain model obtained from the Zubal Phantom data [44]. The model has a pixel size of 2.2 mm, with dimensions of 98×98 pixels, resulting in a square FOV with a length of 21.56 cm. Permittivity and conductivity values are assigned based on data from the IT'IS Foundation [45] at the specified operating frequency. The background outside the brain is considered as air. The actual distribution of permittivity and conductivity are shown in Figs. 3(a) and (b), respectively.

The first simulation compares the performance of homogeneous background inversion and inhomogeneous background inversion. The prior information of permittivity and conductivity is depicted in Figs. 3(c) and (d), respectively. For homogeneous background inversion, the prior information is used as the initial guess, while for inhomogeneous background inversion, it is considered as the background. When utilized as the background, the prior information reduces the contrast in object pixels, resulting in a reduction in the nonlinearity of the inverse problem and an improvement in reconstruction quality.

The reconstructed permittivity and conductivity after 600 iterations are shown in Fig. 4, specifically in (a) and (b), where the prior information serves as an initial guess, and in (c) and (d), where the prior information acts as an inhomogeneous background.

It can be seen that (c) and (d) are more aligned with the actual values of the electrical properties of the brain slice. Not only are the values closer to the actual ones, but the structure of the brain slice is also more clearly represented, resulting in a higher resolution.

It should be noted that inhomogeneous background inversion does not increase computational complexity since the only difference lies in $\bar{\bar{G}}_D$ in Equation (8). This inhomogeneous Green's function can be calculated only once and then stored for later use in minimizing (12).

To quantitatively evaluate the reconstructed image quality, the relative error R_e is adopted, which is defined as

$$R_e = \frac{\| \bar{\bar{\varepsilon}}_r^{act} - \bar{\bar{\varepsilon}}_r^{rec} \|}{\| \bar{\bar{\varepsilon}}_r^{act} \|} \tag{13}$$

where $\bar{\bar{\varepsilon}}_r^{act}$ and $\bar{\bar{\varepsilon}}_r^{rec}$ represent the actual and reconstructed relative permittivities, respectively. A reduction in R_e indicates a closer alignment of the reconstructed image with the actual profile. The trajectory of R_e as a function of the iterations is shown in Fig. 5. It is obvious that at 600 iterations, the R_e of the inhomogeneous background inversion is gradually smaller than the R_e of the homogeneous background inversion with an initial guess. This trend signifies that the inhomogeneous

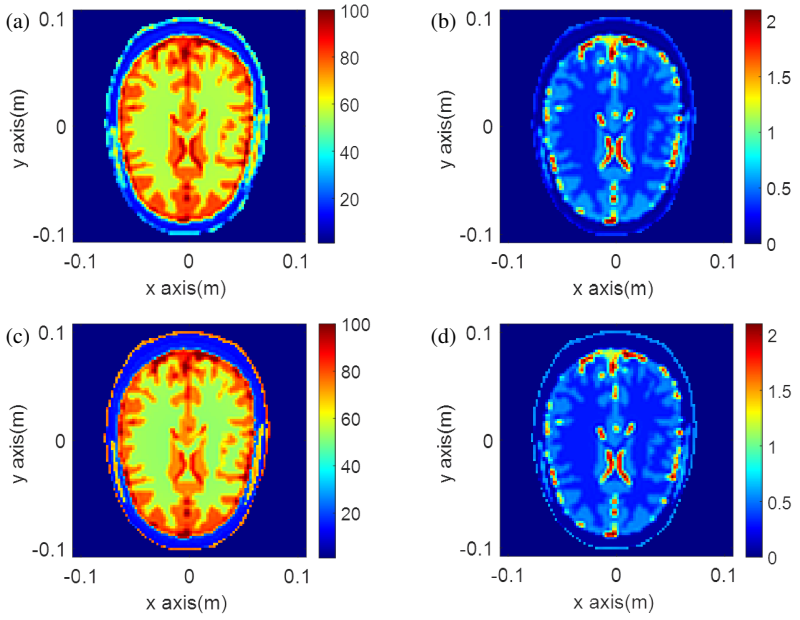

FIGURE 4. The reconstructions with prior information as an initial guess and an inhomogeneous background. (a) and (b) show reconstructions with prior information as an initial guess, while (c) and (d) show reconstructions with prior information as an inhomogeneous background.

TABLE 1. Comparison of the R_e and the Computation Time for the Homogeneous and Inhomogeneous Background Inversion after 600 Iterations.

Methods	R_e	Time (min)
Homogeneous inversion	0.27	130
Inhomogeneous inversion	0.24	126

background inversion can enhance the fidelity of reconstruction. As mentioned earlier, despite the improvement in quality, inhomogeneous background inversion does not require a longer inversion time than homogeneous background inversion. Table 1 presents a comparison of R_e and computation time for both methods. It can be seen that after 600 iterations, the R_e of inhomogeneous background inversion is slightly smaller than that of homogeneous background inversion, while the computation time remains nearly the same. Both methods took approximately 2.1 hours to complete 600 iterations. We notice that since the measurement domain and the expansion basis function practiced in MR-EPT are different from those practiced in CSI, the computational time for MR-EPT will be naturally longer than a CSI solver for an inverse scattering problem of the same dimension. These computations were undertaken on a desktop featuring an AMD 5600X CPU operating at 3.70 GHz, coupled with 32 GB of RAM.

While the inhomogeneous background inversion can improve image quality, it still takes a considerable long time if we aim to obtain high-quality reconstruction results. Fortunately, there might not always be a need for high-quality reconstruction of the entire domain. Instead, high-quality reconstruction may be only required for a specific refinement area. The inhomogeneous background inversion offers the flexibility of achieving a fast refinement area inversion.

Figures 6(a) and (b) depict the reconstructed permittivity and conductivity obtained after 200 iterations of inhomogeneous background inversion. Compared with Fig. 4, specifically Fig. 4(a) and Fig. 4(b), it is obvious that Figs. 6(a) and (b) are rougher, due to insufficient iteration steps. However, this reconstruction result can be utilized to localize the refinement area and serve as a new background for subsequent refinement area inversion. Assuming the refinement area is enclosed by a white dashed line, the new inhomogeneous background is determined based on this refinement area, as depicted in Fig. 6(c) and (d). The new inhomogeneous Green's function is computed by the forward solver. Subsequently, the proposed approach inversion is conducted within the refinement area. The reconstructed permittivity and conductivity are shown in Figs. 6(e) and (f). It can be seen that the resolution of the image in the refinement area can still be significantly improved, indicating the efficacy and feasibility of the refinement-based inversion.

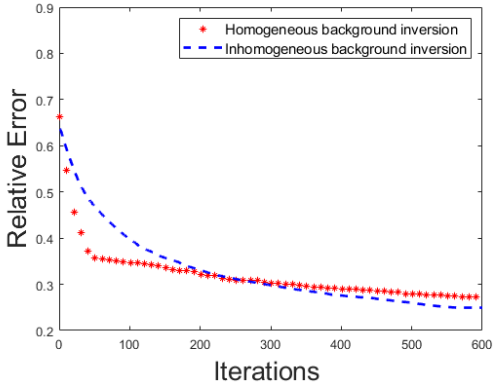

FIGURE 5. The trajectory of R_e as a function of iterations in both homogeneous and inhomogeneous background inversions.

The trajectory of R_e as a function of iterations in both inhomogeneous background inversion and the refinement-based inversion is illustrated in Fig. 7.

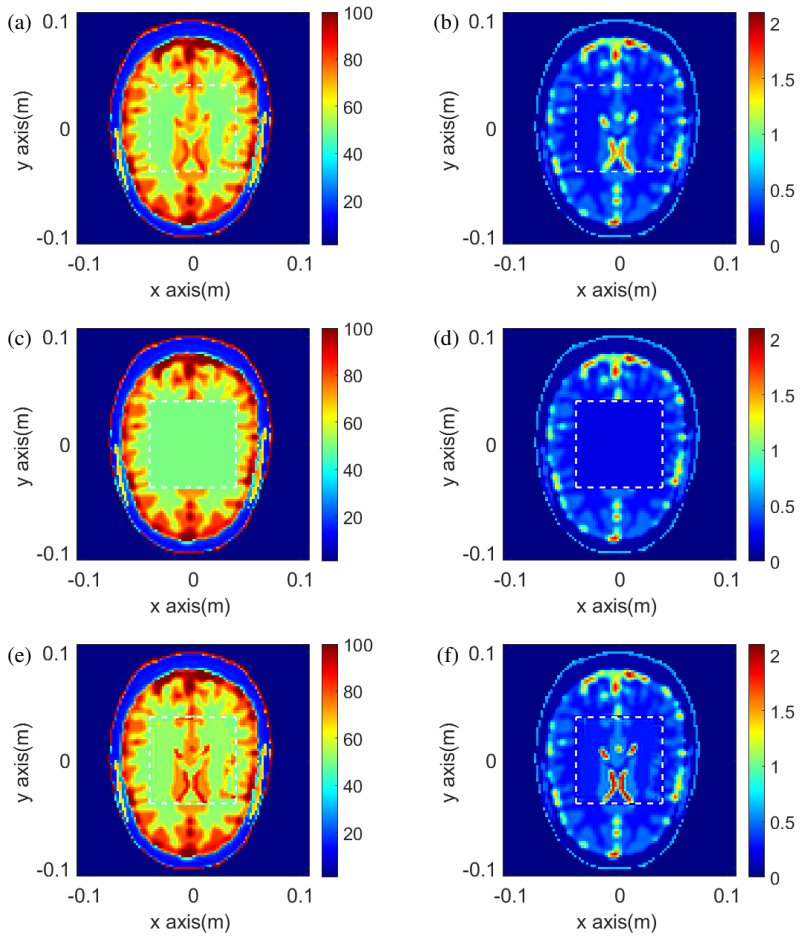

FIGURE 6. The reconstructions by the refinement-based inversion. (a) and (b) are coarse reconstructed permittivity and conductivity in the entire domain; (c) and (d) are the permittivity and conductivity of the new inhomogeneous background for the refinement area inversion; (e) and (f) fine reconstructed permittivity and conductivity in the refinement area.

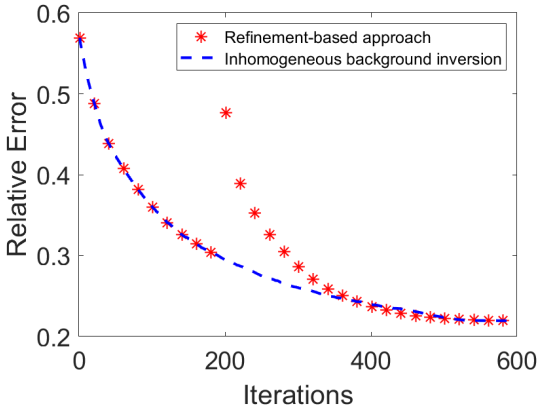

FIGURE 7. The trajectory of R_e as a function of iterations in both inhomogeneous background inversion and the refinement-based inversion.

During the initial 200 iterations, both methods follow a same inversion procedure, resulting in the same R_e values. However, after this initial period, a notable divergence in their convergence trajectories becomes evident. While the inhomogeneous background inversion continues its convergence process, the refinement-based inversion relocates its focus to a specific refinement area. It can be seen that the refinement-based inversion converges more rapidly than the inhomogeneous background inversion. Table 2 presents a comparison of the R_e and computation time of these two methods. At the end of 600 iterations, both methods yield a same R_e value, yet the refinement-based inversion requires only 35% of the computation time compared to the inhomogeneous background inversion approach. It should be noted that the R_e calculation in this example only considers the meshes within the refinement area. Furthermore, it is worth mentioning that the refinement-based inversion spends substantial computational resources during

TABLE 2. Comparison of R_e and computation time for inhomogeneous background inversion and refinement-based inversion after 600 iterations.

Methods	R_e	Time (min)	
		First 200 Iterations	Last 400 Iterations
Inhomogeneous Inversion	0.22	42	84
Refinement-Based Inversion	0.22	42	2.5

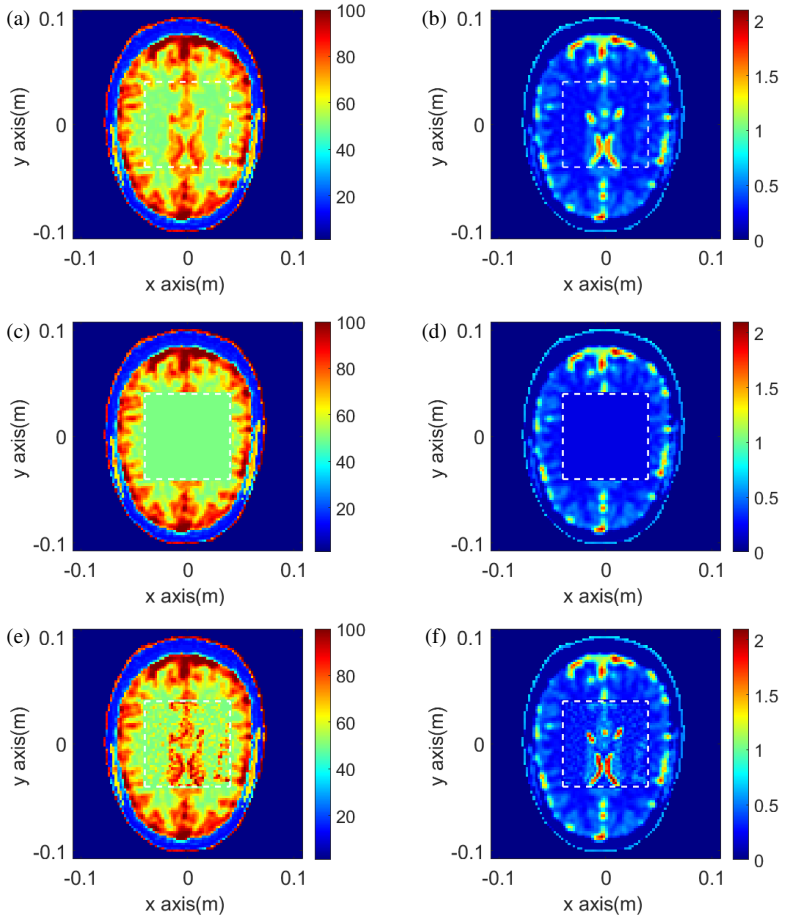

FIGURE 8. The reconstructions by the refinement-based inversion with 10% noise. (a) and (b) are coarse reconstructed permittivity and conductivity in the entire domain; (c) and (d) are the permittivity and conductivity of the new inhomogeneous background for refinement area inversion; (e) and (f) fine reconstructed permittivity and conductivity in the refinement area.

the initial 200 iterations encompassing the entire FOV. In comparison, the subsequent 400 iterations, focusing on the refinement area, demand only 2.5 minutes. This duration accounts for only 3% of the computational time consumed in inhomogeneous background inversion. This means that a significant reduction of the inversion domain can bring higher efficiency and flexibility to MR-EPT applications.

In order to test the robustness against noise, 10% additive white Gaussian noise (AWGN) is added to the $B_1^{+,s}$ data in (7). Other parameters remain unchanged compared with the noise-free case. The reconstruction by the refinement-based inversion under noise scenario is shown in Fig. 8. Same with the noise-free example, the inhomogeneous background inversion with 200 iterations is conducted to provide a rough permittivity and conductivity, as shown in Figs. 8(a) and (b) which show the coarse reconstructed permittivity and conductivity in the entire domain.

Compared to Figs. 6(a) and (b), the reconstruction is slightly distorted by the noise. This distorted reconstruction is then chosen as the new background for subsequent refinement area inversion, depicted in Figs. 8(c) and (d), respectively. Then, the reconstructed relative permittivity and conductivity in the refinement area are shown in Figs. 8(e) and (f). It can be seen that the refinement-based inversion can still successfully reconstruct the electrical properties with accuracy and high resolution, despite the slight distortion caused by noise. The R_e of the reconstruction under noise is 0.24, indicating good robustness against noise. Comparing Fig. 8(e) with Fig. 8(f), the latter appears less sensitive to noise. This is attributed to the brain slice's large loss tangent, where noise has a stronger influence on permittivity compared to conductivity.

5. CONCLUSION

In this paper, we propose a novel FE-BI approach for the inhomogeneous background inversion of MR-EPT. The motivation behind this approach stems from the fact that in reality, we often focus on specific domains rather than the entire region, which can significantly speed up the inversion process by narrowing the inversion domain. Huygens' principle in inhomogeneous background inversion enables us to effectively narrow down the inversion domain. The concept of inhomogeneous background inversion is one of the key components in the refinement-based inversion algorithm. Compared to homogeneous background inversion, inhomogeneous background inversion integrates prior information more effectively, resulting in higher reconstruction quality without increasing computational load. Importantly, the FE-BI formulation of the inho-

mogeneous background inversion allows us to determine the inversion domain more flexibly. Building upon this flexibility, the refinement-based inversion is then introduced. It is stressed that the proposed refinement mechanism with inhomogeneous background is significantly different from prevailing refinement mechanism, since the Huygens' principle is employed to account for the electromagnetic response of the external inhomogeneous medium. This approach utilizes a coarse reconstruction obtained through the inversion of inhomogeneous background inversion across the entire FOV to identify the refinement area and establish a new inhomogeneous background. The subsequent reconstruction within the refinement area achieves a comparable quality to inversion using inhomogeneous background inversion over the entire FOV while significantly reducing computational time. This indicates that the refinement-based inversion combines the efficiency of the local method with the imaging quality of the global method, enhancing the flexibility for clinical applications.

The performance of the proposed FE-BI approach was evaluated through numerical experiments on the reconstruction of a brain slice. The results demonstrated that the inhomogeneous background inversion, using prior information as an inhomogeneous background, outperforms homogeneous background inversion which uses prior information as an initial guess. Additionally, the results also show the feasibility and efficiency of the refinement-based approach, which exhibits a significant advantage in terms of computation time. Furthermore, the robustness against noise of the refinement-based approach was tested under a 10% noise scenario, demonstrating its stability in noisy environments. Future work will focus on generalizing the FE-BI approach to 3D cases and on improving reconstruction efficiency through machine learning and integration with other MRI images. It is noteworthy that extending the method to 3D cases poses significant computational challenges, and overcoming these bottlenecks will be critical for successful implementation.

APPENDIX A.

Convert Equation (4) into "weak" form by multiplying a testing function T and performing an integration over D

$$\begin{aligned}&\iint_D (\nabla T \cdot \nabla E_z^s - k_0^2 \tilde{\varepsilon}_b(\vec{r}) T E_z^s) ds \\ &= \iint_D T w ds + \oint_{\partial D} T \frac{\partial E_z^s}{\partial n} d\Gamma \end{aligned} \tag{A1}$$

The bilinear basis function $\mathcal{B}$ for rectangular cells is chosen as both the testing function and expansion function [43]. The domain D is discretized into a total number of N_{mesh} rectangular-cell meshes. The number of interior nodes is denoted as N_{int}, and the number of nodes located on the boundary ∂D is denoted as N_{bou}. Therefore, we have

$$E_z^s(\vec{r}) = \sum_{n=1}^{N_{int}} e_{z,n}^{s,int} \mathcal{B}_n(\vec{r}) + \sum_{n=N_{int}+1}^{N_{int}+N_{bou}} e_{z,n}^{s,bou} \mathcal{B}_n(\vec{r}) \tag{A2}$$

where $\mathcal{B}_n(\vec{r})$ denotes the basis function centered at node n, while $e_{z,n}^{int}$ and $e_{z,n}^{bou}$ represent the value of scattered electrical field in that node. Obviously, the scattered field at the boundary ∂D is given by

$$E_z^{s,bou}(l) = \sum_{n=N_{int}+1}^{N_{int}+N_{bou}} e_{z,n}^{s,bou} \mathcal{B}_n(l) \tag{A3}$$

Then, the induced current is also expanded by the bilinear basis function, leading to

$$w(\vec{r}) = \sum_{n=1}^{N_{int}+N_{bou}} w_n \mathcal{B}_n(\vec{r}) \tag{A4}$$

where w_n denotes the value of induced current in the nth node.

Additionally, let J^{bou} represent the shorthand for $\frac{\partial E_z^s}{\partial n}$. The expression for J^{bou} can be expanded in basis function as

$$J^{bou}(l) = \sum_{n=1}^{N_{bou}} j_n^{bou} \tilde{\mathcal{B}}_n(l) \tag{A5}$$

where $\tilde{\mathcal{B}}_n(l)$ denotes the piecewise-constant basis function, and j_n^{bou} denotes the its coefficient.

Substituting Equations (A2)–(A5) into Equation (A1) yields the resulting equation in matrix form

$$\begin{aligned}&\begin{bmatrix} \bar{\bar{X}}^{int} & \bar{\bar{X}}^{cros,A} \\ \bar{\bar{X}}^{cros,B} & \bar{\bar{X}}^{bou} \end{bmatrix} \cdot \begin{bmatrix} \bar{e}_z^{s,int} \\ \bar{e}_z^{s,bou} \end{bmatrix} \\ &= \begin{bmatrix} \bar{\bar{Z}}^{int} & \bar{\bar{Z}}^{cros,A} \\ \bar{\bar{Z}}^{cros,B} & \bar{\bar{Z}}^{bou} \end{bmatrix} \cdot \bar{w} + \begin{bmatrix} \bar{0} \\ \bar{\bar{Y}} \cdot \bar{j}^{bou} \end{bmatrix} \end{aligned} \tag{A6}$$

where $\bar{\bar{X}}^{int}$, $\bar{\bar{X}}^{cros,A}$, $\bar{\bar{X}}^{cros,B}$, and $\bar{\bar{X}}^{int}$ have the common form

$$\bar{\bar{X}}_{mn} = \iint_D (\nabla \mathcal{B}_m \cdot \nabla \mathcal{B}_n - k_0^2 \varepsilon_b(\vec{r}) \mathcal{B}_m \mathcal{B}_n) ds \tag{A7}$$

$$\bar{\bar{Z}}_{mn} = \iint_D \mathcal{B}_m \mathcal{B}_n ds \tag{A8}$$

$\bar{\bar{Y}}$ is given by

$$\bar{\bar{Y}}_{mn} = \oint_{\partial D} \mathcal{B}_m \tilde{\mathcal{B}}_n d\partial D \tag{A9}$$

As for the boundary integration, substituting Equations (A2)–(A5) into Equation (6), there is

$$\bar{\bar{L}} \cdot \bar{e}_z^{s,bou} + \bar{\bar{M}} \cdot \bar{j}^{bou} = 0 \tag{A10}$$

where the matrices $\bar{\bar{L}}$ and $\bar{\bar{M}}$ can be found in [43].

Moreover, as for Equation (7), there is

$$B^{+,s} = \frac{1}{2}(B_x^s + iB_y^s) = \frac{1}{i2\omega}\left(\frac{\partial E_z^s}{\partial y} - i\frac{\partial E_z^s}{\partial x}\right) \tag{A11}$$

where B_x^s and B_y^s represent the x and y components of the scattered magnetic field, respectively. Substituting Equation (A2) into Equation (A11) and converting it into a matrix form, there is

$$\bar{b}^{+,s} = \begin{bmatrix} \bar{\bar{P}}^{int} \\ \bar{\bar{P}}^{bou} \end{bmatrix} \cdot \begin{bmatrix} \bar{e}_z^{int} \\ \bar{e}_z^{bou} \end{bmatrix} \tag{A12}$$

where

$$\bar{\bar{P}}^{int} = \frac{1}{i2\omega} \left[\sum_{n=1}^{N_{int}} e_{z,n}^{s,int} \left(\frac{\partial \mathcal{B}_n}{\partial y} - i \frac{\partial \mathcal{B}_n}{\partial x} \right) \right] \tag{A13}$$

$$\bar{\bar{P}}^{bou} = \frac{1}{i2\omega} \left[\sum_{n=N_{int}+1}^{N_{int}+N_{bou}} e_{z,n}^{s,bou} \left(\frac{\partial \mathcal{B}_n}{\partial y} - i \frac{\partial \mathcal{B}_n}{\partial x} \right) \right] \tag{A14}$$

In order to obtain the inhomogeneous Green's function $\bar{\bar{G}}_D$ in domain D, we combine Equations (A6) and (A10), and there is

$$\begin{bmatrix} \bar{\bar{X}}^{int} & \bar{\bar{X}}^{cros,A} \\ \bar{\bar{X}}^{cros,B} & \bar{\bar{X}}^{bou} + \bar{\bar{Y}} \cdot \bar{\bar{M}}^{-1} \cdot \bar{\bar{L}} \end{bmatrix} \bar{e}_z^s = \begin{bmatrix} \bar{\bar{Z}}^{int} & \bar{\bar{Z}}^{cros,A} \\ \bar{\bar{Z}}^{cros,B} & \bar{\bar{Z}}^{bou} \end{bmatrix} \cdot \bar{w} \tag{A15}$$

Therefore, $\bar{\bar{G}}_D$ can be obtained by

$$\bar{\bar{G}}_D = \begin{bmatrix} \bar{\bar{X}}^{int} & \bar{\bar{X}}^{cros,A} \\ \bar{\bar{X}}^{cros,B} & \bar{\bar{X}}^{bou} + \bar{\bar{Y}} \cdot \bar{\bar{M}}^{-1} \cdot \bar{\bar{L}} \end{bmatrix}^{-1} \cdot \begin{bmatrix} \bar{\bar{Z}}^{int} & \bar{\bar{Z}}^{cros,A} \\ \bar{\bar{Z}}^{cros,B} & \bar{\bar{Z}}^{bou} \end{bmatrix} \tag{A16}$$

REFERENCES

[1] Zhang, X., J. Liu, and B. He, "Magnetic-resonance-based electrical properties tomography: A review," *IEEE Reviews in Biomedical Engineering*, Vol. 7, 87–96, 2014.

[2] Liu, J., Y. Wang, U. Katscher, and B. He, "Electrical properties tomography based on B1 maps in MRI: Principles, applications, and challenges," *IEEE Transactions on Biomedical Engineering*, Vol. 64, No. 11, 2515–2530, Nov. 2017.

[3] Leijsen, R., W. Brink, C. van den Berg, A. Webb, and R. Remis, "Electrical properties tomography: A methodological review," *Diagnostics*, Vol. 11, No. 2, 176, Jan. 2021.

[4] Borsic, A., I. Perreard, A. Mahara, and R. J. Halter, "An inverse problems approach to MR-EPT image reconstruction," *IEEE Transactions on Medical Imaging*, Vol. 35, No. 1, 244–256, Jan. 2016.

[5] Katscher, U. and C. A. T. van den Berg, "Electric properties tomography: Biochemical, physical and technical background, evaluation and clinical applications," *NMR in Biomedicine*, Vol. 30, No. 8, e3729, 2017.

[6] Hosseini, S. M. and A. A. Shishegar, "Mapping MRI intensity to the dielectric properties of body tissues using microwave imaging," *IEEE Transactions on Antennas and Propagation*, Vol. 71, No. 8, 6744–6752, 2023.

[7] Haacke, E. M., L. S. Petropoulos, E. W. Nilges, and D. H. Wu, "Extraction of conductivity and permittivity using magnetic resonance imaging," *Physics in Medicine & Biology*, Vol. 36, No. 6, 723, 1991.

[8] Wen, H., "Noninvasive quantitative mapping of conductivity and dielectric distributions using RF wave propagation effects in high-field MRI," in *Medical Imaging 2003: Physics of Medical Imaging*, Vol. 5030, 471–477, San Diego, California, United States, Jun. 2003.

[9] Voigt, T., U. Katscher, and O. Doessel, "Quantitative conductivity and permittivity imaging of the human brain using electric properties tomography," *Magnetic Resonance in Medicine*, Vol. 66, No. 2, 456–466, 2011.

[10] Ammari, H., H. Kwon, Y. Lee, K. Kang, and J. K. Seo, "Magnetic resonance-based reconstruction method of conductivity and permittivity distributions at the larmor frequency," *Inverse Problems*, Vol. 31, No. 10, 105001, 2015.

[11] Gurler, N. and Y. Z. Ider, "Gradient-based electrical conductivity imaging using MR phase," *Magnetic Resonance in Medicine*, Vol. 77, No. 1, 137–150, Jan. 2017.

[12] Wang, Y., P.-F. van de Moortele, and B. He, "Automated gradient-based electrical properties tomography in the human brain using 7 Tesla MRI," *Magnetic Resonance Imaging*, Vol. 63, 258–266, Nov. 2019.

[13] Hafalir, F. S., O. F. Oran, N. Gurler, and Y. Z. Ider, "Convection-reaction equation based magnetic resonance electrical properties tomography (cr-MREPT)," *IEEE Transactions on Medical Imaging*, Vol. 33, No. 3, 777–793, Mar. 2014.

[14] Yildiz, G. and Y. Z. Ider, "Use of dielectric padding to eliminate low convective field artifact in cr-MREPT conductivity images," *Magnetic Resonance in Medicine*, Vol. 81, No. 5, 3168–3184, May 2019.

[15] Balidemaj, E., C. A. T. van den Berg, J. Trinks, A. L. H. M. W. van Lier, A. J. Nederveen, L. J. A. Stalpers, H. Crezee, and R. F. Remis, "CSI-EPT: A contrast source inversion approach for improved MRI-based electric properties tomography," *IEEE Transactions on Medical Imaging*, Vol. 34, No. 9, 1788–1796, Sep. 2015.

[16] Leijsen, R. L., W. M. Brink, C. A. T. van den Berg, A. G. Webb, and R. F. Remis, "3-D contrast source inversion-electrical properties tomography," *IEEE Transactions on Medical Imaging*, Vol. 37, No. 9, 2080–2089, Sep. 2018.

[17] Arduino, A., L. Zilberti, M. Chiampi, and O. Bottauscio, "CSI-EPT in presence of RF-shield for MR-coils," *IEEE Transactions on Medical Imaging*, Vol. 36, No. 7, 1396–1404, Jul. 2017.

[18] Arduino, A., O. Bottauscio, M. Chiampi, and L. Zilberti, "Magnetic resonance-based imaging of human electric properties with phaseless contrast source inversion," *Inverse Problems*, Vol. 34, No. 8, 084002, 2018.

[19] Leijsen, R. L., W. M. Brink, A. G. Webb, and R. F. Remis, "Effects of simulated error-sources on different 3-D CSI-EPT strategies," *IEEE Transactions on Computational Imaging*, Vol. 7, 713–723, 2021.

[20] Serrallés, J. E. C., I. I. Giannakopoulos, B. Zhang, C. Ianniello, M. A. Cloos, A. G. Polimeridis, J. K. White, D. K. Sodickson, L. Daniel, and R. Lattanzi, "Noninvasive estimation of electrical properties from magnetic resonance measurements via global maxwell tomography and match regularization," *IEEE Transactions on Biomedical Engineering*, Vol. 67, No. 1, 3–15, Jan. 2020.

[21] Eda, N., M. Fushimi, K. Hasegawa, and T. Nara, "A method for electrical property tomography based on a three-dimensional integral representation of the electric field," *IEEE Transactions on*

Medical Imaging, Vol. 41, No. 6, 1400–1409, Jun. 2022.

[22] Hong, R., S. Li, J. Zhang, Y. Zhang, N. Liu, Z. Yu, and Q. H. Liu, "3-D MRI-based electrical properties tomography using the volume integral equation method," *IEEE Transactions on Microwave Theory and Techniques*, Vol. 65, No. 12, 4802–4811, Dec. 2017.

[23] Giannakopoulos, I. I., J. E. C. Serrallés, L. Daniel, D. K. Sodickson, A. G. Polimeridis, J. K. White, and R. Lattanzi, "Magnetic-resonance-based electrical property mapping using Global Maxwell Tomography with an 8-channel head coil at 7 Tesla: A simulation study," *IEEE Transactions on Biomedical Engineering*, Vol. 68, No. 1, 236–246, Jan. 2021.

[24] Georgakis, I. P., I. I. Giannakopoulos, M. S. Litsarev, and A. G. Polimeridis, "A fast volume integral equation solver with linear basis functions for the accurate computation of EM fields in MRI," *IEEE Transactions on Antennas and Propagation*, Vol. 69, No. 7, 4020–4032, Jul. 2021.

[25] Berg, Van den P. M. and R. E. Kleinman, "A contrast source inversion method," *Inverse Problems*, Vol. 13, No. 6, 1607, 1997.

[26] Van den Berg, P. and A. Abubakar, "Contrast source inversion method: State of art," *Progress In Electromagnetics Research*, Vol. 34, 189–218, 2001.

[27] Nie, Z., F. Yang, Y. Zhao, and Y. Zhang, "Variational born iteration method and its applications to hybrid inversion," *IEEE Transactions on Geoscience and Remote Sensing*, Vol. 38, No. 4, 1709–1715, Jul. 2000.

[28] Inda, A. J. G., S. Y. Huang, N. İmamoğlu, and W. Yu, "Physics-coupled neural network magnetic resonance electrical property tomography (MREPT) for conductivity reconstruction," *IEEE Transactions on Image Processing*, Vol. 31, 3463–3478, 2022.

[29] Inda, A. J. G., S. Y. Huang, N. İmamoğlu, R. Qin, T. Yang, T. Chen, Z. Yuan, and W. Yu, "Physics informed neural networks (PINN) for low snr magnetic resonance electrical properties tomography (MREPT)," *Diagnostics*, Vol. 12, No. 11, 2627, Oct. 2022.

[30] Qin, R., A. J. G. Inda, Z. Zhou, Y. Enomoto, T. Yang, N. İmamoğlu, J. Gomez-Tames, S. Huang, and W. Yu, "REC-NN: A reconstruction error compensation neural network for Magnetic Resonance Electrical Property Tomography (MREPT)," in *2023 45th Annual International Conference of the IEEE Engineering in Medicine & Biology Society (EMBC)*, 1–4, Sydney, Australia, 2023.

[31] Ruan, G., Z. Wang, C. Liu, L. Xia, H. Wang, L. Qi, and W. Chen, "Magnetic resonance electrical properties tomography based on modified physics-informed neural network and multi-constraints," *IEEE Transactions on Medical Imaging*, Vol. 43, No. 9, 3263–3278, 2024.

[32] Yin, W., W. Yang, and H. Liu, "A neural network scheme for recovering scattering obstacles with limited phaseless far-field data," *Journal of Computational Physics*, Vol. 417, 109594, 2020.

[33] Gao, Y., H. Liu, X. Wang, and K. Zhang, "On an artificial neural network for inverse scattering problems," *Journal of Computational Physics*, Vol. 448, 110771, 2022.

[34] Chen, X., *Computational Methods for Electromagnetic Inverse Scattering*, John Wiley Sons Singapore Pte. Ltd., Singapore, 2018.

[35] Chen, X., "Subspace-based optimization method for inverse scattering problems with an inhomogeneous background medium," *Inverse Problems*, Vol. 26, No. 7, 074007, 2010.

[36] Jin, J.-M., *The Finite Element Method in Electromagnetics*, John Wiley & Sons, 2015.

[37] Zakaria, A., C. Gilmore, and J. LoVetri, "Finite-element contrast source inversion method for microwave imaging," *Inverse Problems*, Vol. 26, No. 11, 115010, 2010.

[38] Zakaria, A. and J. LoVetri, "The finite-element method contrast source inversion algorithm for 2D transverse electric vectorial problems," *IEEE Transactions on Antennas and Propagation*, Vol. 60, No. 10, 4757–4765, 2012.

[39] Zakaria, A., A. Baran, and J. LoVetri, "Estimation and use of prior information in FEM-CSI for biomedical microwave tomography," *IEEE Antennas and Wireless Propagation Letters*, Vol. 11, 1606–1609, 2013.

[40] Abubakar, A., W. Hu, P. M. van den Berg, and T. M. Habashy, "A finite-difference contrast source inversion method," *Inverse Problems*, Vol. 24, No. 6, 065004, 2008.

[41] Sacolick, L. I., F. Wiesinger, I. Hancu, and M. W. Vogel, "B1 mapping by bloch-siegert shift," *Magnetic Resonance in Medicine*, Vol. 63, No. 5, 1315–1322, 2010.

[42] Yarnykh, V. L., "Actual flip-angle imaging in the pulsed steady state: A method for rapid three-dimensional mapping of the transmitted radiofrequency field," *Magnetic Resonance in Medicine*, Vol. 57, No. 1, 192–200, Jan. 2007.

[43] Peterson, A. F., S. L. Ray, and R. Mittra, *Computational Methods for Electromagnetics*, IEEE Press, New York, 1998.

[44] Zubal, I. G., C. R. Harrell, E. O. Smith, Z. Rattner, G. Gindi, and P. B. Hoffer, "Computerized three-dimensional segmented human anatomy," *Medical Physics*, Vol. 21, No. 2, 299–302, Feb. 1994.

[45] Gabriel, C. and S. Gabriel, "Compilation of the dielectric properties of body tissues at RF and microwave frequencies," Tech. Rep. N.AL/OE-TR-1996-0037, Occupational and Environmental Health Directorate, Radiofrequency Radiation Division, Brooks Air Force Base, Texas, USA, 1996.